Geophysical and Geochemical Evidence for Deep Temperature Variations Beneath Mid-Ocean Ridges

Colleen A. Dalton *et al.*

Science **344**, 80 (2014);
DOI: 10.1126/science.1249466

This copy is for your personal, non-commercial use only.

If you wish to distribute this article to others, you can order high-quality copies for your colleagues, clients, or customers by clicking here.

Permission to republish or repurpose articles or portions of articles can be obtained by following the guidelines here.

The following resources related to this article are available online at www.sciencemag.org (this information is current as of April 4, 2014):

Updated information and services, including high-resolution figures, can be found in the online version of this article at:
http://www.sciencemag.org/content/344/6179/80.full.html

Supporting Online Material can be found at:
http://www.sciencemag.org/content/suppl/2014/04/02/344.6179.80.DC1.html

A list of selected additional articles on the Science Web sites **related to this article** can be found at:
http://www.sciencemag.org/content/344/6179/80.full.html#related

This article **cites 37 articles**, 9 of which can be accessed free:
http://www.sciencemag.org/content/344/6179/80.full.html#ref-list-1

This article has been **cited by** 1 articles hosted by HighWire Press; see:
http://www.sciencemag.org/content/344/6179/80.full.html#related-urls

This article appears in the following **subject collections:**
Geochemistry, Geophysics
http://www.sciencemag.org/cgi/collection/geochem_phys

Downloaded from www.sciencemag.org on April 4, 2014

Science (print ISSN 0036-8075; online ISSN 1095-9203) is published weekly, except the last week in December, by the American Association for the Advancement of Science, 1200 New York Avenue NW, Washington, DC 20005. Copyright 2014 by the American Association for the Advancement of Science; all rights reserved. The title *Science* is a registered trademark of AAAS.

Either J_2 and C_{22} are fortuitously close to having ratio 10/3, or the nonhydrostatic contributions are small because of compensation (f is small). The degree-3 gravity, uncontaminated by tides and rotation, provides an estimate: $f_{30} \cong 115.3/349 \cong 0.33$, implying an Airy depth of compensation of ~32 km. This would in turn imply $f_{20} \cong 0.23$ (and f_{22} should equal f_{20} if compensation is isotropic); hence, the part of C_{22} arising from the topographic excess is $\sim 43 \times 10^{-6}$. Assuming that the hydrostatic contribution to this harmonic is then the remainder, 1507×10^{-6}, we infer that the most likely moment of inertia (MOI) of Enceladus is $0.336MR^2$, where M is the mass and R is the radius (*9*). If we choose the value of $f_{20} = f_{22}$ such that the hydrostatic part of J_2 is exactly 10/3 the hydrostatic part of C_{22}, we obtain $f \cong 0.27$, implying a depth of compensation of ~37 km and a moment of inertia of $\sim 0.335MR^2$.

If we instead use an iterative approach to self-consistently separate the hydrostatic and nonhydrostatic parts of both gravity and topography [(*9*), section S3.5], we obtain converging estimates of f_{20} and f_{22} (~0.25) when the moment of inertia is $0.335MR^2$, suggesting a compensation depth of ~34 km. The convergent $f_{20} = f_{22}$ is close to the value predicted on the basis of the observed f_{30}, confirming that the assumption of isotropic compensation is reasonable.

When we included elastic flexure as a means of supporting topography in our model, we found that in order to be consistent with the observed gravity-to-topography ratios, the elastic thickness must be less than 0.5 km, a value consistent with other estimates made from flexural analysis (*13*) and relaxation studies (*14*).

Results in this MOI range are compatible with a differentiated structure (*15*). For example, a value of $0.335MR^2$ can arise from a model with a relatively low core density of ~2.4 g/cm^3 and a H_2O mantle of density of 1 g/cm^3 and thickness of 60 km (*9*). The high heat flow and plume activity strongly suggests a differentiated structure, which is compatible with these results.

The data imply a great deal of compensation; if our assumption of Airy isostasy is correct, the inferred compensation depth of 30 to 40 km is most simply explained as the thickness of the ice shell overlying a liquid water layer. The large compensation excludes a very different kind of model, in which the main effect is the tidal and rotational response of a body with a nonradial symmetry of material properties. The tidal and rotational response of a body with a degree-1 variation in properties could introduce topography and gravity at degree 3, an example of mode coupling (*16*); but if this were responsible for the topographic distortion, then it would predict a much larger gravity distortion than is observed (yielding $f \sim 1$ instead of the observed much smaller values). For the same reason, a frozen-in tidal and rotational bulge from an earlier epoch (*17*) will not explain the observed gravity if that bulge has persisted in the ice mantle. A frozen-in deformation of the core (*18*) could in principle explain the gravity, but the topography would still have to be highly compensated.

The presence of at least a regional south polar subcrustal sea suggests a model in which the mean temperature of the ice beneath the south pole is warmer than elsewhere, perhaps leading to a lower mean density of ~1% (corresponding to 100 K temperature excess and a coefficient of thermal expansion of $\sim 10^{-4}$ K^{-1}). But to satisfy the observed gravity, it is then necessary to insert a region of higher-density material roughly twice as large as that needed to offset the topographic depression alone and at a depth at least as great as the previous compensation depth estimates. If this material is water and is 8% denser than the surrounding ice, then a layer ~10 km thick is required, diminishing in thickness toward the lower southern latitudes. The total hydrostatic pressure at the base of this region would be in balance with the pressure at the same depth, plausibly at or near the base of the ice shell, in adjacent non–south polar regions that lack water, thus reducing the tendency for this layer to spread laterally. A highly concentrated mass anomaly at the south pole would predict $J_3 = -J_{2,\mathrm{nh}}$. The data (Table 2) suggest $J_3 \sim -0.35J_{2,\mathrm{nh}}$, and this could be explained by a mass anomaly that extends from the pole to roughly 50° south latitude (*9*). However, the limitations of the data preclude high confidence in this inference.

Although the gravity data cannot rule out a global ocean, a regional sea is consistent with the gravity, topography, and high local heat fluxes (*19*) and does not suffer from the thermal problems that a global ocean encounters (*19*, *20*). A global ocean would yield larger and potentially detectable longitudinal librations than are predicted for a solid body (*21*). The gravity coefficients and inferred MOI of Enceladus are not consistent with a forced 4:1 secondary libration (*17*, *22*) at the 2σ level (*9*).

References and Notes

1. J. N. Spitale, C. C. Porco, *Nature* **449**, 695–697 (2007).
2. F. Postberg, J. Schmidt, J. Hillier, S. Kempf, R. Srama, *Nature* **474**, 620–622 (2011).
3. J. R. Spencer *et al.*, *Science* **311**, 1401–1405 (2006).
4. M. M. Hedman *et al.*, *Nature* **500**, 182–184 (2013).
5. C. J. A. Howett, J. R. Spencer, J. Pearl, M. Segura, *J. Geophys. Res.* **116**, (E3), E03003 (2011).
6. J. Meyer, J. Wisdom, *Icarus* **188**, 535–539 (2007).
7. G. W. Ojakangas, D. J. Stevenson, *Icarus* **66**, 341–358 (1986).
8. K. Zhang, F. Nimmo, *Icarus* **204**, 597–609 (2009).
9. Materials and methods are available as supplementary materials on *Science* Online.
10. L. Iess *et al.*, *Science* **327**, 1367–1369 (2010).
11. L. Iess *et al.*, *Science* **337**, 457–459 (2012).
12. F. Nimmo, B. G. Bills, P. C. Thomas, *J. Geophys. Res.* **116**, E11001 (2011).
13. B. Giese *et al.*, *Geophys. Res. Lett.* **35**, L24204 (2008).
14. M. T. Bland, K. N. Singer, W. B. McKinnon, P. M. Schenk, *Geophys. Res. Lett.* **39**, L17204 (2012).
15. G. Schubert, J. D. Anderson, B. J. Travis, J. Palguta, *Icarus* **188**, 345–355 (2007).
16. S. Zhong *et al.*, *J. Geophys. Res.* **39**, L15201 (2012).
17. C. C. Porco *et al.*, *Science* **311**, 1393–1401 (2006).
18. W. B. McKinnon, *J. Geophys. Res.* **118**, 1775 (2013).
19. G. Tobie, O. Cadek, C. Sotin, *Icarus* **196**, 642–652 (2008).
20. J. H. Roberts, F. Nimmo, *Icarus* **194**, 675–689 (2008).
21. N. Rambaux, J. C. Castillo-Rogez, J. G. Williams, Ö. Karatekin, *Geophys. Res. Lett.* **37**, L04202 (2010).
22. J. Wisdom, *Astron. J.* **128**, 484–491 (2004).

Acknowledgments: L.I., M.P., M.D., and P.T. acknowledge support from the Italian Space Agency. D.H., F.N., and J.I.L. are grateful to NASA for support through the Cassini Project. The work of R.A.J., J.W.A., and S.W.A. was carried out at the Jet Propulsion Laboratory, California Institute of Technology, under a contract with NASA. The Doppler data and ancillary information used in this analysis are archived in NASA's Planetary Data System.

Supplementary Materials
www.sciencemag.org/content/344/6179/78/suppl/DC1
Materials and Methods
Supplementary Text
Figs. S1 to S6
Tables S1 to S7
References (*23*–*36*)

8 January 2014; accepted 24 February 2014
10.1126/science.1250551

Geophysical and Geochemical Evidence for Deep Temperature Variations Beneath Mid-Ocean Ridges

Colleen A. Dalton,[1]*† **Charles H. Langmuir,**[2] **Allison Gale**[2,3]

The temperature and composition of Earth's mantle control fundamental planetary properties, including the vigor of mantle convection and the depths of the ocean basins. Seismic wave velocities, ocean ridge depths, and the composition of mid-ocean ridge basalts can all be used to determine variations in mantle temperature and composition, yet are typically considered in isolation. We show that correlations among these three data sets are consistent with 250°C variation extending to depths >400 kilometers and are inconsistent with variations in mantle composition at constant temperature. Anomalously hot ridge segments are located near hot spots, confirming a deep mantle-plume origin for hot spot volcanism. Chemical heterogeneity may contribute to scatter about the global trend. The coherent temperature signal provides a thermal calibration scale for interpreting seismic velocities located distant from ridges.

Mantle convection controls the evolution of the planet's interior and results in the motion of tectonic plates. The characteristics of this convection are governed by the density and viscosity of the mantle, which are functions of both temperature and composition.

Two sets of observations that can constrain these properties are the velocity of seismic shear waves (V_S) and the geochemistry of mid-ocean ridge basalts (MORBs). Outstanding controversies about the interpretation of both data sets have historically prevented definitive advances in understanding the relative importance of variations in temperature and composition beneath ridges. V_S can be imaged throughout the entire mantle (*1*, *2*) and is strongly sensitive to temperature (*3*), potentially providing critical constraints on global temperature variations. However, factors other than temperature, including composition (*4*), partial melt (*5*), volatiles (*6*), and anelasticity (*3*), also affect V_S, producing large discrepancies in estimates of upper-mantle temperature (*3*, *7*, *8*). Early studies of global variations in the depth of ocean ridges and the major-element composition of MORBs indicated temperature variations of 220° ± 40°C beneath ridges to mantle depths >200 km (*9*, *10*). Yet subsequent studies have emphasized the importance of mantle composition (*11*, *12*) and melt-transfer processes (*13*, *14*) in these data sets and inferred smaller temperature variations (50° to 60°C).

To overcome the limitations associated with each data set, the seismological, petrological, and bathymetric data sets can be jointly analyzed (*15*). Earlier attempts to compare seismic models and ridge observations, using 34 global locations (*16*) or 39 locations along the Mid-Atlantic Ridge (MAR) (*17*), identified correlations only for mantle depths <200 km and inferred along-ridge temperature variations that were confined to the shallow mantle. The correlations at lithospheric depths, however, must be approached with caution, because the lateral averaging inherent in seismic models introduces an artificial spreading-rate dependence into V_S at shallow depths due to thicker lithosphere near the ridges at slow spreading rates. This issue, when considered together with the lack of correlation at depths >200 km, casts doubt on the conclusion reached by these studies that temperature plays an important role.

We performed a comprehensive global comparison of variations in V_S beneath ridges, axial ridge depth (D_R), and MORB chemistry. To facilitate comparison between the geophysical and geochemical observations, we examined variations at the scale of discrete ridge segments. Individual

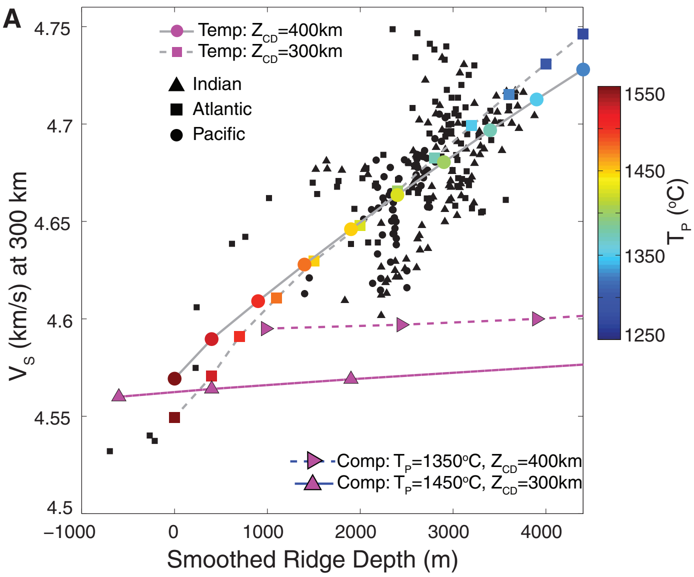

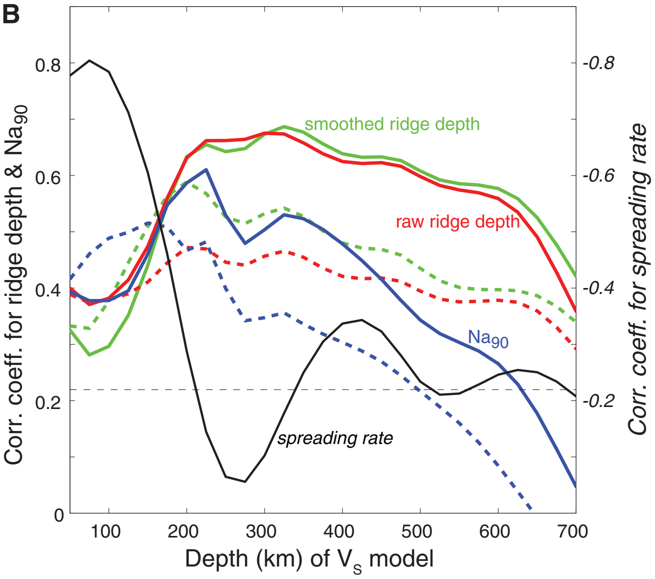

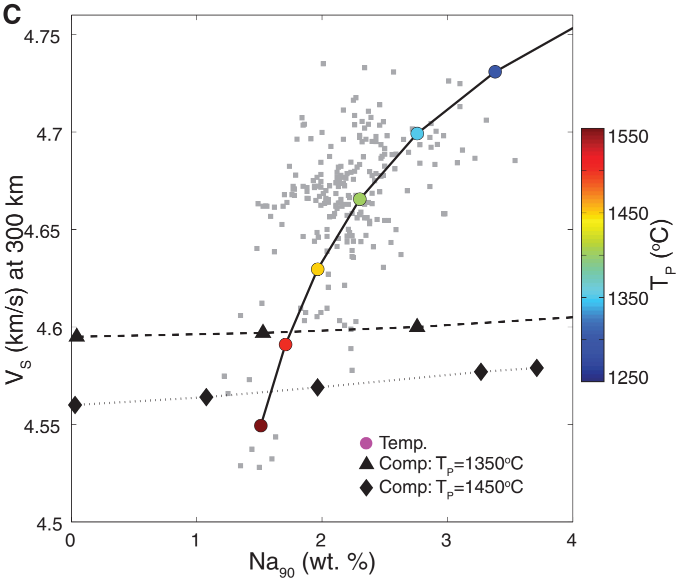

Fig. 1. Comparison of ridge observations and V_S. (**A**) Black symbols: D_R and V_S (*1*) at 300 km depth beneath the ridge for 242 nodes evenly spaced along the six longest ridge systems: the Mid-Atlantic Ridge (MAR), Southwest Indian Ridge (SWIR), Central Indian Ridge (CIR), Southeast Indian Ridge (SEIR), Pacific-Antarctic Ridge (PAR), and East Pacific Rise (EPR). D_R for each node was calculated from a weighted average of the mean depths of nearby segments within a 550-km radius. Colored circles and squares: predictions for variable T_P for Z_{CD} = 300 km and 400 km. V_S was calculated using (*3*), with grain size = 2 cm. Colored triangles: predictions for variable composition for Z_{CD} = 300 km and 400 km at T_P = 1350°C and 1450°C. Elastic V_S was calculated using Perple_X (*21*) and the thermodynamic database of (*28*). (**B**) Correlation coefficient *r* with V_S. Blue lines: correlation with Na_{90} in 225 segments. Red lines: correlation with 584 raw D_R values. Green lines: correlation with 242 smoothed D_R values. Dashed lines: only D_R values 1 to 4 km or Na_{90} > 1.8 are used. Thin horizontal dashed line: value of *r* that can be resolved from zero at significance level = 0.001 (196 degrees of freedom). Solid black line: negative correlation between V_S and spreading rate (*29*). (**C**) Comparison of observed and predicted relationships between Na_{90} and V_S at 300 km depth for temperature variations (colored symbols) and variations in mantle composition at temperatures of 1350°C and 1450°C (black symbols). Na_{90} was predicted using (*10*). V_S prediction is described in (A).

---

[1]Department of Earth and Environment, Boston University, 685 Commonwealth Avenue, Boston, MA 02215, USA. [2]Department of Earth and Planetary Sciences, Harvard University, 20 Oxford Street, Cambridge, MA 02138, USA. [3]Department of Plant and Earth Science, University of Wisconsin, River Falls, 410 South 3rd Street, River Falls, WI 54022, USA.

*Corresponding author. E-mail: colleen_dalton@brown.edu
†Present address: Department of Geological Sciences, Brown University, 324 Brook Street, Box 1846, Providence, RI 02912, USA.

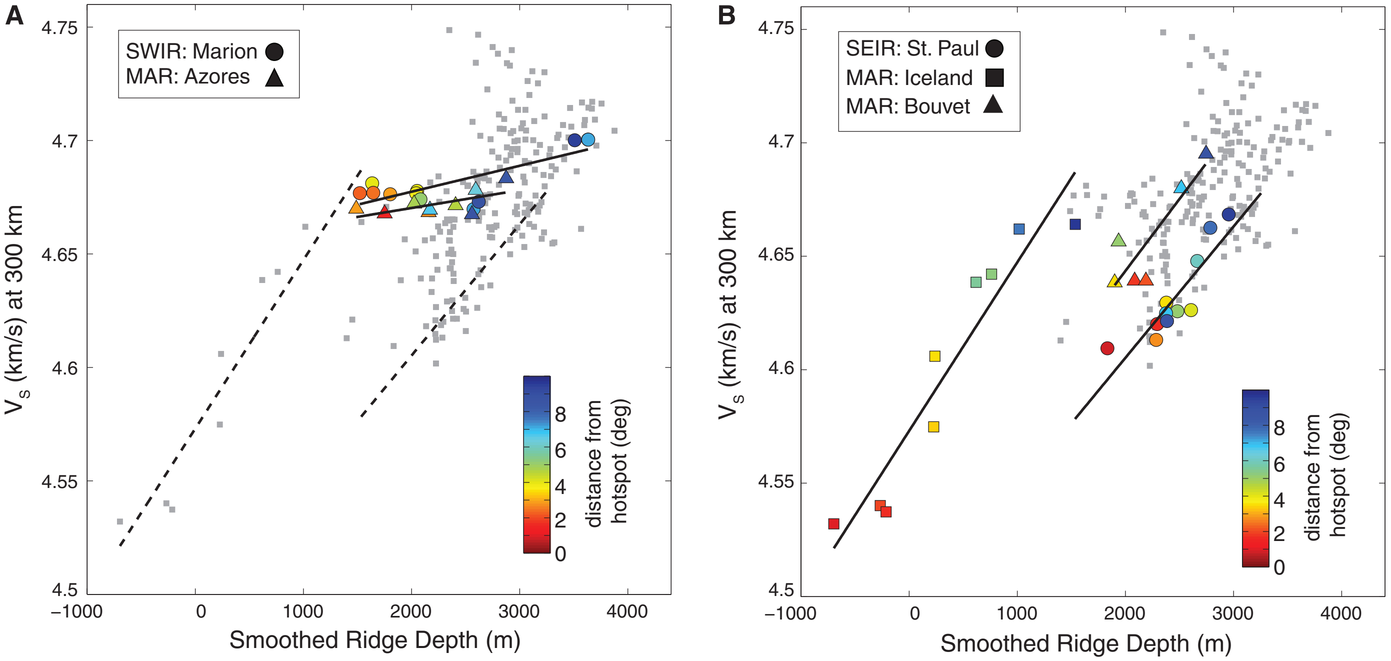

Fig. 2. Observed D_R and V_S at 300 km. (**A**) Segments located <10° (1100 km) from the Marion and Azores hot spots color-coded by distance from those hot spots. Solid black lines: best-fitting lines. Dashed black lines: best-fitting lines for St. Paul and Iceland from (B). (**B**) As in (A) but for the St. Paul, Iceland, and Bouvet hot spots.

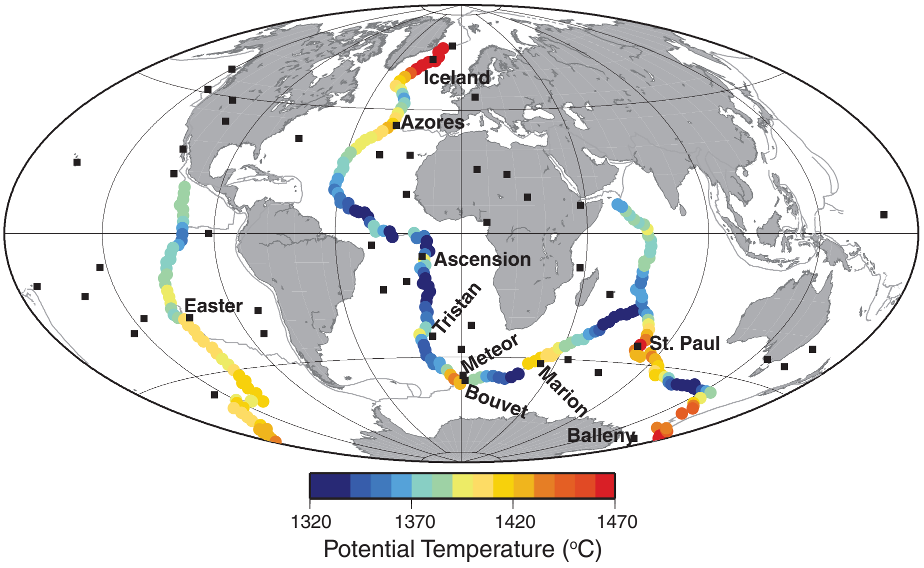

Fig. 3. Along-ridge variation in T_P. Averages of T_P estimated separately from D_R and V_S at 300 km are shown. Temperature differs by <20°C from these averaged T_P values for 82% of locations when estimated from D_R alone and for 93% of locations when estimated from V_S alone. Shallow D_R values near Azores and Marion give the illusion of slightly elevated temperatures, which is inconsistent with the mantle V_S values (Fig. 2A). Black squares: hot spots from (*30*) plus St. Paul/Amsterdam. Hot spots mentioned in the text are labeled.

segments at the level of approximately second-order segmentation features (*18*) were identified using multi-resolution bathymetry in GeoMapApp (www.geomapapp.org), yielding 771 ridge segments totaling 60,864 km in length (fig. S1A). Geochemical variations along the ridge were obtained from a global data set of major- and trace-element concentrations for 16,694 MORB samples (*19*) that were corrected for low-pressure fractionation (see the supplementary materials and fig. S1B). Isotropic V_S along the ridges was sampled from the S40RTS model (*1*) at 242 nodes evenly spaced along the six longest ridge systems (fig. S1C).

The data show a strong correlation between D_R and V_S in the mantle beneath the ridge globally (Fig. 1A). The correlation coefficient is >0.6 at depths of 200 to 550 km, with a maximum at 325 km (Fig. 1B). This correlation is not dominated by the end-member points; Fig. 1B provides correlation coefficients calculated using only D_R values of 1 to 4 km. Comparison of V_S and Na_{90}, performed for the entire fractionation-corrected data set excluding back-arc spreading centers, also reveals a statistically significant correlation (Fig. 1C and fig. S23). This correlation is strongest at 225 km and is >0.4 for mantle depths of 150 to 450 km. Other compositional parameters, including Ca_{90}/Al_{90} and Fe_{90}, also co-vary with V_S, D_R, and Na_{90} (figs. S16 to S21). We focus on depths >200 km to avoid artifacts related to the spreading-rate dependence of V_S (Fig. 1B and supplementary text S2).

The robust correlations in Fig. 1 suggest that long-wavelength variations in D_R, V_S, and MORB composition are controlled by a common mechanism. Furthermore, the depth extent of the correlations (>400 km) is much greater than previously recognized. Earlier studies, for which significant correlations were found only at depths <200 km, suffered from limited sampling [(*16*, *17*) fig. S1B] and the use of low-resolution seismic models. When modern seismic models are used, the correlations at shallow depths identified by (*16*, *17*) vanish, and strong correlations at depths >200 km emerge (figs. S10 and S11).

We consider two end-member explanations for the new observations: (i) mantle temperature variations at constant composition and (ii) mantle compositional variations at constant temperature. The likely origin of large-scale variations in mantle composition is the extraction of basalt at ocean ridges and preferential recycling of basalt through subduction; mantle compositional variations are therefore modeled on this basis. For prediction of V_S and D_R, each ridge segment is treated as an isostatically balanced column containing four layers: water, crust, residual mantle, and fertile mantle. Each column is characterized by a mantle potential temperature (T_P) and composition that extend from the Moho to the isostatic compensation depth (Z_{CD}). Overburden pressure at Z_{CD} is assumed to be constant for all columns, allowing water-layer thickness to be determined (supplementary text S4 and figs. S13 and S14). Petrological modeling was performed using MELTS (*20*) and the approach of (*10*), and V_S was predicted using (*3*) for temperature variations and (*21*) for compositional variations (supplementary text S5 and S6).

We find that the observed global variations in V_S, D_R, and MORB chemistry are consistent with 200° to 250°C variation in mantle T_P, extending to 300 to 400 km (Fig. 1, A and C). Predicted D_R, V_S, and Na_{90} all vary inversely with T_P. Shallow ridges at high temperatures reflect the combined effects of thicker ocean crust and less-dense mantle. Petrological modeling of Fe_{90}, Na_{90}, and Ca_{90}/Al_{90} indicates a temperature range of 1300° to 1550°C, showing a remarkable consistency for temperature estimates from the three independent methods (supplementary text S6 and figs. S16 and S17).

In contrast, mantle compositional variations produced by linear mixing of basalt and peridotite predict flat relationships between V_S and D_R and V_S and Na_{90} that are inconsistent with the positive trend of the observations (Fig. 1), and also predict relationships between Na_{90}-Fe_{90} and Ca_{90}/Al_{90}-Fe_{90} and Fe_{90}-D_R (figs. S16 to S20) that are not consistent with the dominant trend of the observations.

Although the principal component of variation is consistent with mantle temperature variations, compositional variations produce trends orthogonal to the principal correlations and should explain some of the scatter about the global trend. For example, ridge segments near the Azores and Marion hot spots have large variations in D_R at nearly constant V_S (Fig. 2A). This flat relationship between D_R and Vs is consistent with a compositional origin for the Azores and Marion rises (*22*). Depleted peridotite in the underlying mantle provides a source of buoyancy that elevates the ridge segments. This conclusion is further supported by the distinctly low Fe_{90} of the Azores ridge segments (*23*), which indicates a depleted source. For other hot spots, such as Iceland, Bouvet, and St. Paul, V_S and D_R increase with distance from the hot spot along lines oriented subparallel to the global trend (Fig. 2B and figs. S24 to S29). The offset of these three trends indicates that a factor in addition to mantle temperature must influence D_R or Vs, but with existing geochemical data it is not clear whether the offsets are produced by changes in mantle composition.

The temperature calibration in Fig. 1A allows T_P along the entire ridge system to be estimated (Fig. 3). Excluding segments with $D_R < 1$ km, the global range of T_P is 1314° to 1464°C, with 1355°C and 1408°C as the first and third quartile. High T_P values in the Atlantic and Indian basins are located near hot spots, especially when considered relative to the regional background value. Locations near the Iceland, Ascension, Tristan, Meteor, Bouvet, St. Paul, and Balleny hot spots are characterized by temperatures 30° to 60°C above the regional background temperature. These are large-scale regional averages; temperatures immediately beneath the hot spots may be much higher. The fact that the warm ridge segments are all located near known hot spots lends strong support to the hypothesis that volcanism at these hot spots is caused by mantle plumes originating in the transition zone or lower mantle (*24*). Detection of plumes with global tomography suggests that plume material may be deflected horizontally at sublithospheric depths, thus distributing the thermal anomaly over a broad area surrounding the conduit (*2*). The global range of temperature variations is reduced to 100° to 150°C when only ridge segments located >700 km from hot spots are considered (fig. S8). We find no temperature anomaly associated with the Azores and Marion hot spots, nor with the Easter hot spot in the Pacific basin, where high spreading rates along the East Pacific Rise may readily mix plume and ambient mantle.

Low temperatures are found at 105° to 135°E along the Southeast Indian Ridge (SEIR), overlapping with the Australian-Antarctic Discordance, where seismic studies (*25*, *26*) have imaged high velocities that have been attributed to a convective downwelling in the mantle (*27*). The two other low-temperature zones identified here—2° to 30°S along the MAR and 55° to 80°E along the Southwest Indian Ridge (SWIR)—are characterized by high V_S values >4.7 km/s at 300 km depth and may indicate additional colder regions occupying the upper mantle.

This study demonstrates that the global long-wavelength variations in the surface expression of mid-ocean ridges—bathymetry and MORB major-element composition—are governed primarily by the temperature of the mantle extending several hundreds of kilometers below the surface. The scatter about the global trend may originate from major-element heterogeneity in the mantle; from imperfections and incompleteness in the petrological and seismological data sets; or from complexities that we have not considered, including volatiles in the mantle, melt-transfer processes, dynamic topography, and buoyancy-driven flow. The principal finding reported here is the consistency of temperatures estimated from V_S, D_R, and MORB compositions, which provides a uniform calibration of mantle temperature that could be applied to V_S worldwide. Although composition or partial melt may influence V_S in certain regions, much of the global seismic-velocity signal in regions distant from ocean ridges probably reflects variations in upper-mantle potential temperature.

References and Notes

1. J. Ritsema, A. Deuss, H. J. van Heijst, J. H. Woodhouse, *Geophys. J. Int.* **184**, 1223–1236 (2011).
2. S. French, V. Lekic, B. Romanowicz, *Science* **342**, 227–230 (2013).
3. U. H. Faul, I. Jackson, *Earth Planet. Sci. Lett.* **234**, 119–134 (2005).
4. C.-T. Lee, *J. Geophys. Res.* **108**, JB002413 (2003).
5. W. C. Hammond, E. D. Humphreys, *J. Geophys. Res.* **105**, 10975–10986 (2000).
6. S. Karato, H. Jung, *Earth Planet. Sci. Lett.* **157**, 193–207 (1998).
7. K. Priestley, D. McKenzie, *Earth Planet. Sci. Lett.* **244**, 285–301 (2006).
8. Y. Yang, D. W. Forsyth, D. S. Weeraratne, *Earth Planet. Sci. Lett.* **258**, 260–268 (2007).
9. E. M. Klein, C. H. Langmuir, *J. Geophys. Res.* **92**, 8089–8115 (1987).
10. C. H. Langmuir, E. M. Klein, T. Plank, in *Mantle Flow and Melt Generation at Mid-Ocean Ridge* (American Geophysical Union, Washington, DC, 1992), pp. 183–280.
11. Y. Shen, D. W. Forsyth, *J. Geophys. Res.* **100**, 2211–2237 (1995).
12. Y. Niu, M. J. O'Hara, *J. Petrol.* **49**, 633–664 (2008).
13. M. L. Collier, P. B. Kelemen, *J. Petrol.* **51**, 1913–1940 (2010).
14. J.-I. Kimura, S. Sano, *J. Petrol.* **53**, 1637–1671 (2012).
15. D. A. Wiens, K. A. Kelley, T. Plank, *Earth Planet. Sci. Lett.* **248**, 30–42 (2006).
16. E. Humler, J. L. Thirot, J. P. Montagner, *Nature* **364**, 225–228 (1993).
17. Y.-S. Zhang, T. Tanimoto, E. M. Stolper, *Phys. Earth Planet. Inter.* **84**, 79–93 (1994).
18. K. C. Macdonald *et al.*, *Nature* **335**, 217–225 (1988).
19. A. Gale, C. A. Dalton, C. H. Langmuir, Y. Su, J.-G. Schilling, *Geochem. Geophys. Geosyst.* **14**, 489–518 (2013).
20. P. D. Asimow, M. S. Ghiorso, *Am. Mineral.* **83**, 1127–1131 (1998).
21. J. A. D. Connolly, *Geochem. Geophys. Geosyst.* **10**, GC002540 (2009).
22. H. Zhou, H. J. B. Dick, *Nature* **494**, 195–200 (2013).
23. A. Gale, S. Escrig, E. J. Gier, C. H. Langmuir, S. L. Goldstein, *Geochem. Geophys. Geosyst.* **12**, GC004334 (2011).
24. W. J. Morgan, *Nature* **230**, 42–43 (1971).
25. D. W. Forsyth, R. L. Ehrenbard, S. Chapin, *Earth Planet. Sci. Lett.* **84**, 471–478 (1987).
26. M. H. Ritzwoller, N. M. Shapiro, G. M. Leahy, *J. Geophys. Res.* **108**, JB002522 (2003).
27. M. Gurnis, R. D. Müller, L. Moresi, *Science* **279**, 1499–1504 (1998).
28. W. C. Xu, C. Lithgow-Bertelloni, L. Stixrude, J. Ritsema, *Earth Planet. Sci. Lett.* **275**, 70–79 (2008).
29. C. DeMets, R. G. Gordon, D. F. Argus, S. Stein, *Geophys. Res. Lett.* **21**, 2191–2194 (1994).
30. V. Courtillot, A. Davaille, J. Besse, J. Stock, *Earth Planet. Sci. Lett.* **205**, 295–308 (2003).

Acknowledgments: We acknowledge NSF grants OCE-0752166 to C.A.D. and OCE-0752281 to C.H.L. We thank P. Hall, M. Jackson, S. Parman, and M. Ishii for helpful discussions. The major-element MORB data and the catalog of ridge segments are available in the supporting information of (*19*).

Supplementary Materials

www.sciencemag.org/content/344/6179/80/suppl/DC1
Materials and Methods
Supplementary Text
Figs. S1 to S29
Table S1
References (*31*–*38*)

9 December 2013; accepted 24 February 2014
10.1126/science.1249466